



Development of a Computer Numerical Control (CNC)-Integrated Passive Autofocus for Continuous Wood Specimen Imaging Using Frequency-Domain Analysis

Jihoon SONG^{1,2} · Junyoung PARK^{1,2} · Ohkyung KWON^{3,†} · Soo CHUNG^{1,2,4,†}

ABSTRACT

This paper presents a fast Fourier transform-based autofocus technique for computer numerical control microscopy systems for the observation of fine anatomical structures in wood specimens. The proposed method enables systematic pausing of the motorized stage at predetermined X-Y coordinates, analysis of the high-frequency spectral components of the acquired images through fast Fourier transform processing to derive quantitative sharpness metrics, and subsequent implementation of a dual-stage coarse- and fine-search algorithm to determine the optimal Z-axis focal position prior to stage advancement under G-code control. This iterative protocol facilitates continuous focus optimization and ensures consistent image quality across specimens that exhibit inherent variations in surface topography. In addition, an intuitive graphical user interface was developed to provide streamlined operator control of the autofocus parameters and real-time performance monitoring capabilities. Experimental validation demonstrated that the proposed approach achieved a focusing accuracy within 10 μm while consistently generating high-resolution microscopic images across diverse wood specimen types, with the system capable of processing five specimens in a single automated sequence.

Keywords: wood specimen, fast Fourier transform, computer numerical control (CNC), autofocus, microscope, sharpness, G-code

1. INTRODUCTION

Accurate wood-species identification is essential for industrial utilization, illegal-logging enforcement, and fundamental anatomical research. Traditionally, wood anatomists perform visual microscopic examinations to distinguish between species; however, the diversity and

subtle anatomical differences among timbers mean that years of experience are required for reliable identification (Ravindran *et al.*, 2020). This challenge has been faced in recent anatomical studies; for instance, delineation of juvenile and mature wood zones in *Diospyros kaki* requires precise cell-level imaging, underscoring the role of a stable focus in anatomical assessments

Date Received August 18, 2025; Date Revised August 31, 2025; Date Accepted September 19, 2025; Published November 25, 2025

¹ Department of Biosystems Engineering, Seoul National University, Seoul 08826, Korea

² Integrated Major in Global Smart Farm, Seoul National University, Seoul 08826, Korea

³ National Instrumentation Center for Environmental Management, Seoul National University, Seoul 08826, Korea

⁴ Research Institute of Agriculture and Life Sciences, Seoul National University, Seoul 08826, Korea

[†] Corresponding author: Ohkyung KWON (e-mail: Zoom@snu.ac.kr, <https://orcid.org/0000-0002-6307-0060>)

[†] Corresponding author: Soo CHUNG (e-mail: Soochung@snu.ac.kr, <https://orcid.org/0000-0002-1498-7534>)

© Copyright 2025 The Korean Society of Wood Science & Technology. This is an Open-Access article distributed under the terms of the Creative Commons Attribution Non-Commercial License (<http://creativecommons.org/licenses/by-nc/4.0/>) which permits unrestricted non-commercial use, distribution, and reproduction in any medium, provided the original work is properly cited.

(Kartikawati *et al.*, 2024).

Illegal logging, which is estimated to generate 52–157 billion USD annually, drives deforestation and biodiversity loss worldwide (Silva *et al.*, 2022). In addition, the enforcement of regulations, such as CITES, depends on rapid and trustworthy species recognition (Hwang and Sugiyama, 2021). Automated wood identification, which combines high-throughput microscopy, reliable autofocus, and explainable image analysis, is a critical tool in both conservation and commerce. Beyond identification, a consistent focus is required in wood utilization studies, such as the evaluation of teak sapwood for activated carbon production, where precise imaging is essential for interpreting anatomical features (Sutapa *et al.*, 2024).

Deep learning-based approaches have demonstrated promising results in species classification using microscopic wood images (Kwon *et al.*, 2017). For example, a convolutional neural network (CNN) model automatically identified Korean softwood species from transverse section images, achieving competitive accuracy without manual feature extraction. Building on this, ensembles of CNNs were introduced to further improve classification performance (Kwon *et al.*, 2019), which highlighted the importance of large, high-quality image datasets and consistent imaging conditions for robust inference. More recently, the Mask R-CNN has been applied to the instance segmentation of softwood rays, which demonstrated reliable detection and measurement performance with microscopic wood images (Yoo *et al.*, 2022).

These findings underscore that advances in imaging hardware—particularly autofocus-enabled, computer numerical control (CNC) integrated microscopy systems can directly contribute to enhancing AI-driven wood identification by supplying more consistent and sharper images for model training and employment.

Moreover, scanning electron microscopy-based analyses of adhesive bond-line performance have shown that even subtle losses in image clarity can compromise the

interpretation of structural behavior (Kim *et al.*, 2024), and complementary reviews of water vapor diffusion in adhesive layers have emphasized that reliable evaluation of bond-line durability depends on consistent microstructural observations (Zinad and Csiha, 2024).

In South Korea, where timber imports are subject to legal proof under recent regulations (e.g., the 2018 *Act on the Sustainable Use of Timbers* requiring proof of legal origin; Zeitlin and Overdevest, 2021), there remains a shortage of domestic anatomists, microscopy infrastructure, and reference databases, leaving inspection points without the tools needed to verify species instantly. Recent efforts to establish standardized property databases for Korean red pine have further highlighted the critical need for consistent imaging inputs to support reliable reference infrastructures (Park *et al.*, 2024), and the inherently uneven surfaces of wood specimens cause any preset focus to drift as the stage moves to a new area, requiring continuous refocusing to maintain image quality. Such unevenness is a major issue in drying processes, where internal water transport strongly influences defects, and recent work on large-cross-section red pine timber has demonstrated that pretreatment can mitigate these problems (Batjargal *et al.*, 2023).

Moreover, reliable image-based analyses are essential not only for species recognition and sustainability (Hadi *et al.*, 2022) but also for broader material characterization. Studies on clonal teak trees have demonstrated that ImageJ-based anatomical measurements of growth and density rely heavily on image clarity to ensure reproducibility (Nugroho *et al.*, 2024).

To address this problem, our objective was to develop a low-cost, CNC-integrated autofocus module that enables rapid, repeatable focus adjustment across large wood-specimen surfaces. The entire autofocus module was designed for modular CNC integration such that it could be retrofitted to existing microscope stages. The stage executes a simple “move, stop, autofocus, capture, move” loop under standard G-code control, capturing

each coordinate only once the focus has been optimized. This modularity allows large-area tiling with guaranteed focus consistency and eliminates the need for manual refocusing between positions, dramatically increasing throughput in automated wood-imaging workflows.

Autofocus methods can be broadly classified into active and passive approaches (Chen *et al.*, 2010; Peddigari *et al.*, 2005). Active autofocus employs auxiliary optical devices, such as infrared or ultrasonic sensors, to calculate the distance to the specimen surface, providing rapid focus adjustment but requiring additional hardware that increases the system cost.

In contrast, passive autofocus relies solely on image-derived metrics and can be implemented in either the spatial or frequency domains. Spatial-domain techniques evaluate focus quality through measures such as the image Laplacian, which computes the second derivative of the pixel intensity to quantify edge sharpness, and the Sobel operator, which estimates first-order intensity gradients, as well as various statistical methods (Wu *et al.*, 2022).

Frequency-domain methods, on the other hand, apply the fast Fourier transform (FFT) to convert image data into its spectral components. Signal and noise occupy different frequency bands, therefore these methods generally exhibit superior anti-noise performance compared to spatial-domain metrics (Li *et al.*, 2024). By adapting passive autofocus strategies, our CNC-regulated module can maintain optimal focus across micrometre-scale height variations in wood specimens, yielding consistently sharp microscopic images, even on inherently uneven surfaces.

2. MATERIALS and METHODS

2.1. Materials

Wood specimens of various species were cut into rectangular blocks that were 70 mm wide, 20 mm high,

and 40 mm long. The transverse sections of the wood specimens were sanded using sequential application of sandpaper of European standard grit sizes 180, 320, 400, and 600 to obtain a smooth surface. Imaging was performed using a USB camera (OS-CM50, Osunhitech, Goyang, Korea) coupled to a Nikon Plan 4 × / 0.13 phase-contrast microscope objective. Each specimen was mounted on a custom motor-driven XYZ translation stage built around a stepper motor (US-17HS4401S, Usongshine, Shenzhen, China).

Motion commands, formatted as G-codes, were parsed and streamed to the stage controller using the open-source Python libraries *grbl-streamer* (v2.0.2) and *gcode-machine* (v1.0.3) authored by Michael Franzl. Computations were performed on a workstation equipped with a 13th Gen Intel® Core™ i7-13700 CPU (2.10 GHz) and an NVIDIA GeForce RTX 3060 (12 GB) GPU.

2.2. Methods

The wood samples were examined using three principal planes: the transverse [Fig. 1(a)], longitudinal [radial; Fig. 1(b)], and longitudinal planes [Fig. 1(c)]. As illustrated in Fig. 1(a), the transverse plane clearly reveals both the growth-ring anatomy and the boundaries between the heartwood, sapwood, earlywood, and latewood (Arisandi *et al.*, 2023). All microscopic imaging was performed on cross-sections of the wood, because in preliminary trials, we found that using perfectly flat surfaces made observations of the cross-section far easier than using radial or tangential faces, maximizing image clarity and reproducibility.

The GRBL-controlled board drives three stepper-motor axes. The X- and Y-axes translate the workable beneath the z-axis gantry, which carries two aligned cameras. The wood specimens were arranged on the Y-stage and positioned incrementally for imaging purposes.

Each 70 mm × 20 mm sample was scanned along blue

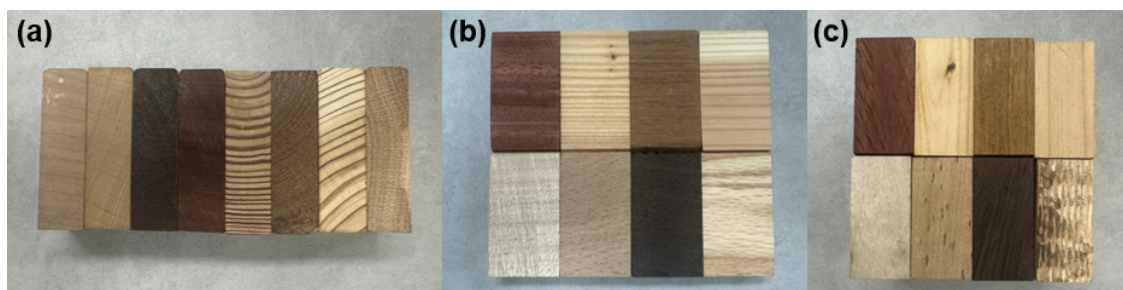


Fig. 1. Photographic overview of the eight wood block specimens used in this study. (a) Transverse, (b) longitudinal (radial), and (c) longitudinal surfaces.

lines from its starting position (red triangle) to its halt position (green squares; Fig. 2). No automatic boundary-recognition procedure was used to define the scan path. Instead, all X-Y target coordinates were specified manually prior to acquisition (via the control GUI), and the specimen positioning was manually adjusted when needed. To control the spacing between consecutively scanned regions and support downstream stitching in future studies, we intentionally introduced an overlap between adjacent tiles. During capturing, subsequent

coordinates were offset by 800 μm along either the X or the Y axis; this fixed step size yielded a small but consistent overlap at the tile boundaries and prevented gaps.

Upon completion of the scanning process for one sample, the head shifted along the X-axis by 20 mm, and the next sample was scanned using the same process, yielding continuous scan coverage of the defined surface to be observed.

To enable real-time blur detection on wood specimen

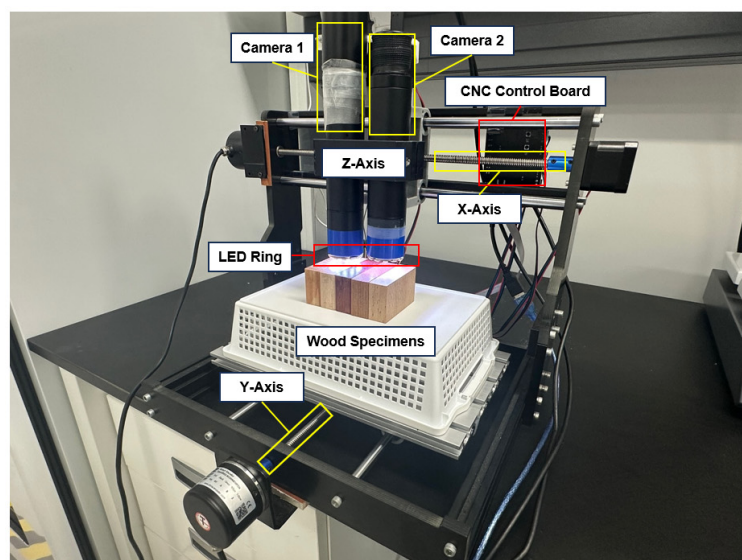


Fig. 2. CNC based wood-surface scanning system and schematic of the wood scan path. CNC: computer numerical control.

surfaces, we implemented a GPU-accelerated sharpness metric based on FFT and a two-stage hill-climbing algorithm using Python. All processing was performed on $1,024 \times 1,024$ -pixel frames using NVIDIA GPUs and the CuPy Library (<https://github.com/cupy/cupy>).

In practice, although we applied FFT due to its efficiency, the underlying mathematical operation used was discrete Fourier transform (DFT). The DFT of an $M \times X$ image $I(x, y)$ is defined as

$$F(k, l) = \sum_{x=0}^{M-1} \sum_{y=0}^{N-1} I(x, y) e^{-j2\pi \left(\frac{kx}{M} + \frac{ly}{N} \right)} \quad (1)$$

Where $I(x, y)$ is the intensity of the input image at pixel $I(x, y)$, M and N are the width and height of the image (in pixels), K and l are the horizontal and vertical frequency indices, respectively; and $j = \sqrt{-1}$ is the

imaginary unit. The direct computation costs $O(M^2N^2)$ operations are prohibitively high for a $1,024 \times 1,024$ frame. In practice, we used the FFT $O((MN) \log(MN))$ algorithm that produces identical results (Changela *et al.*, 2020).

Before applying FFT, we converted any incoming color frame into a single-channel grayscale image, as shown in Fig. 3. This collapsed the RGB channels into luminance, ensuring that the FFT only measured intensity variations (edges and textures) without being skewed by color content, and provided a reduced-complexity representation that eases the computational load and accelerates processing (Lin *et al.*, 2024).

The inverse transform is calculated as follows:

$$I'(x, y) = \frac{1}{MN} \sum_{x=0}^{M-1} \sum_{y=0}^{N-1} F'(k, l) e^{j2\pi \left(\frac{kx}{M} + \frac{ly}{N} \right)} \quad (2)$$

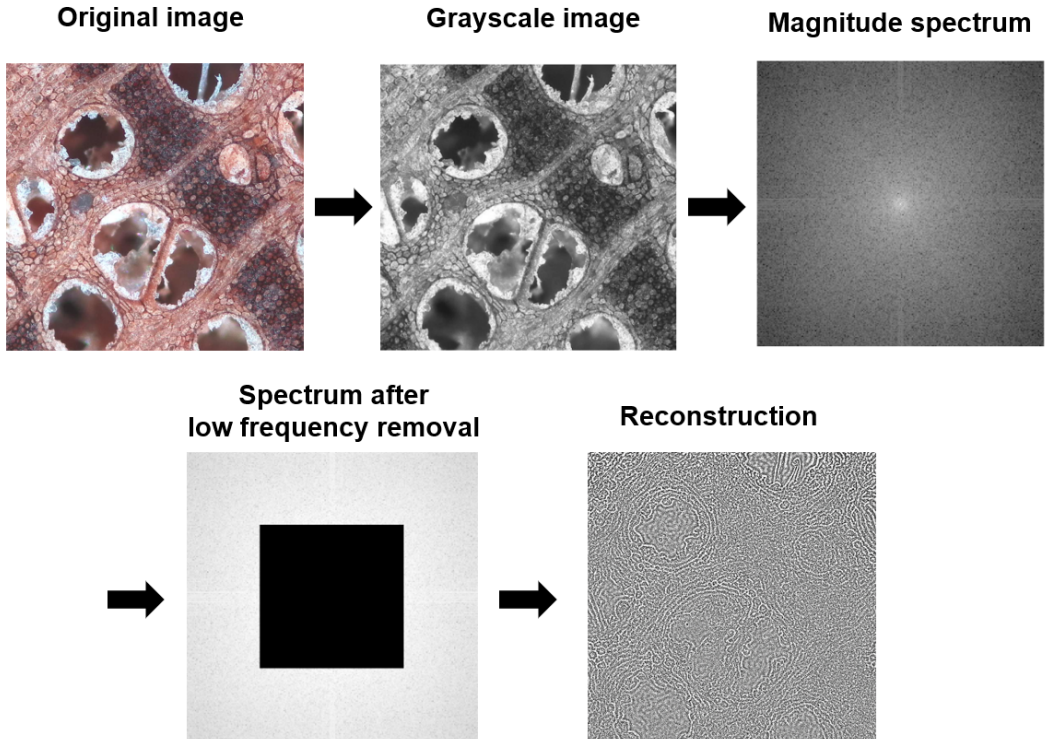


Fig. 3. End to end fast Fourier transform-based blur-emphasis pipeline.

On the GPU, each frame was streamed to the device via memcopyAsync on a non-blocking CUDA stream. Then, we performed the following sequence of spectral operations to suppress blurring and emphasize the edges:

1. Computed the real-input 2D FFT.
2. The zero-frequency component was moved to the center of the spectrum, where it appeared as the brightest point in the magnitude image, which represented the image's overall mean intensity, while the intensities fell radially, indicating higher spatial frequencies as it moves outward.
3. Central low-frequency removal to zero out a square block of coefficients, such that subsequent processing only operated on detail-rich frequencies.
4. Undid the earlier shift, restoring the spectrum's natural indexing.
5. The spatial image $\hat{I}(x, y)$ was reconstructed from the masked spectrum. All very low frequencies are eliminated, therefore the resulting image highlights the edges and fine texture, which is an essential prerequisite for a reliable blur metric.

The zero-frequency component moving process in Step 2 is not mathematically required for the FFT itself, but it significantly improves both visualization and processing convenience. In the raw FFT output, the zero-frequency component is located at the array corners, with the low-frequency information split across the four quadrants. By shifting the zero-frequency component to the center, the spectrum becomes radially symmetrical, with low frequencies concentrated at the center and high frequencies radiating outward. This layout is easier to interpret by humans and allows for simple isotropic masking operations, such as removing a central block of coefficients without having to treat multiple disjoint regions at the array corners.

Next, we compute the focus score S by applying decibel-style compression to the reconstructed amplitude $|\hat{I}(x, y)|$ and averaging over all pixels:

$$S = \frac{1}{MN} \sum_{x=0}^M \sum_{y=0}^{N-1} 20 \log_{10}(|\hat{I}(x, y)| + \epsilon) \quad (3)$$

Where ϵ prevents logarithmic singularities. The $20\log_{10}$ form to express the amplitude compresses the wide dynamic range of the FFT and sensitively reflects even small high-frequency losses, ensuring that blurry frames yield significantly lower scores (Fig. 4).

To locate the optimal focus position, we applied a two-stage hill-climbing search (Jia *et al.*, 2022) along the Z-axis, as shown in Fig. 5. In the coarse search, the stage moves up or down from the initialized Z position in increments of ΔZ coarse, measuring S after each move. It continues in a direction that increases S and halts when no further improvement occurs (either owing to a score drop or exceeding the reversal limits). Then, the fine search repeats this procedure from the coarse result using smaller increases in ΔZ fine, precisely converging on the local maximum of S . The Z-axis step sizes for coarse and fine searches were chosen to match our stage's 1.8° two-phase stepper motors, which move $10 \mu\text{m}$ per pulse, and to exceed the natural jitter of our FFT-based focus score. The $10 \mu\text{m}$ resolution was derived directly from our CNC motor's full step angle attached with a 2 mm lead screw and using the following calculation:

$$\Delta x = 2 \text{ mm} \times \frac{1.8^\circ}{360^\circ} = 0.01 \text{ mm} = 10 \mu\text{m} \quad (4)$$

Although microstepping was used for smooth motor movement, it only smoothed the motor drive currents in the CNC board (Fig. 2) and did not alter the fundamental full-step size of the chosen stepper motor (Bednarski *et al.*, 2021). Therefore, we set the fine-search increment to $\Delta Z = 10 \mu\text{m}$ to prevent consecutive measurements from overlapping within the $\pm 5 \mu\text{m}$ focus jitter window, and we selected ΔZ coarse = 50 μm to reliably bracket the true focus peak in the coarse

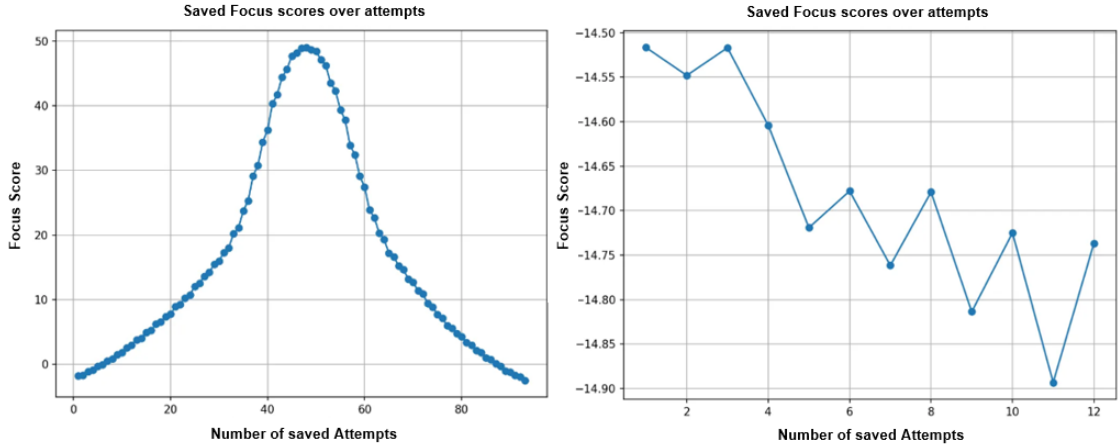


Fig. 4. Saved focus score thresholds over time. The graph on the left is a full sweep of the saved threshold values, showing a clear peak and symmetrical drop-off. The graph on the right side is a zoomed in view of the saved values below 0 db, where the focus-score algorithm’s natural jitter dominates.

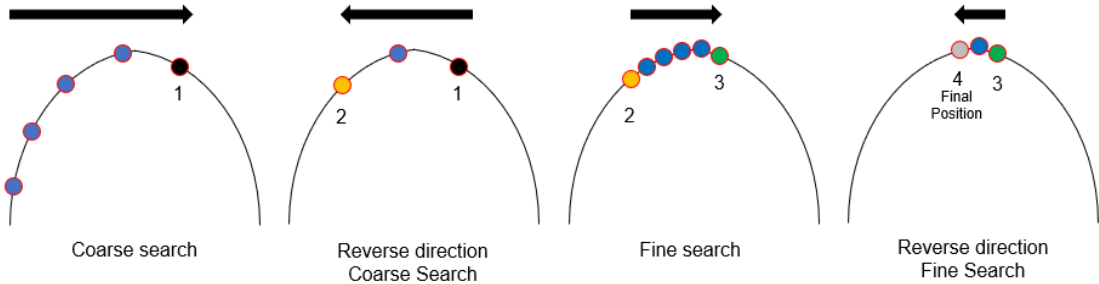


Fig. 5. The four steps of autofocus after the initialization process. 1) Coarse forward scan locates an approximate focus maximum. 2) Reverse coarse scan refines the position from the opposite direction. 3) Fine forward scan around the coarse peak yields a high-precision focus estimate. 4) Reverse fine scan provides the final Z-axis position adjustment.

stage, avoiding unintentional overshooting.

To avoid false starts in the low-score region, autofocus was initiated by loading the saved X and Y coordinates and oscillating the stage up and down until the focus score increased above zero, where our empirically determined boundary beyond which score fluctuations no longer overlapped, before commencing the two-stage hill-climbing routine.

The acceptable sharpness range around the true focal plane is called the lens’s depth of focus (DOF; Young

et al., 1993). Once the Z-axis position fell anywhere within the DOF range, the image quality remained constant. This implies that the fine-search stage does not need to chase the absolute maximum focus score at every micrometer step, and converging into the lens’s DOF is sufficient to guarantee sharp images while minimizing unnecessary Z-axis control.

In this study, the DOF was defined by the following diffraction-based expression:

$$\Delta z = \frac{\lambda}{4 \cdot n \cdot \left(1 - \sqrt{1 - (NA/n)^2}\right)} \quad (5)$$

$$\Delta z \approx \frac{\lambda}{2NA^2} \quad (7)$$

Where λ denotes the wavelength of the (quasi-mono-chromatic) illumination, NA is the objective's numerical aperture, and n represents the refractive index of the medium separating the lens form the specimen. This formulation originates from the diffraction theory, in which the axial range is determined by the point at which the accumulated phase deviation causes the Airy disk to surpass the permissible blur size in the image plane.

When the numerical aperture is moderate ($NA \ll n$, the square-root term can be approximated by a first-order Taylor expansion:

$$\sqrt{1 - (NA/n)^2} \approx 1 - \frac{\left(\frac{NA}{n}\right)^2}{2} \quad (6)$$

Substituting this into Equation (5) yields:

This simplified formula is used for quick estimations, because it avoids the nested square root and closely matches the exact form in the low- to mid- regime. The approximation is valid here because our microscope geometry fixed the distance between the image sensor and the internal optics of the camera. Under this fixed geometry, the DOF refers specifically to the allowable displacement of the image plane (in the sensor space) and should not be confused with the depth of field, which describes the object-space range and scales differently with magnification. The optical setup from the lens to the sensor is rigid, therefore the DOF value computed using Equation (5) (or its simplified form) directly corresponds to the z-axis tolerance in the CNC stage program (Fig. 6).

In our autofocus implementation, this DOF limit was used as a stop condition for fine-stage motion. Once the focus score predicts that the Z position is inside the

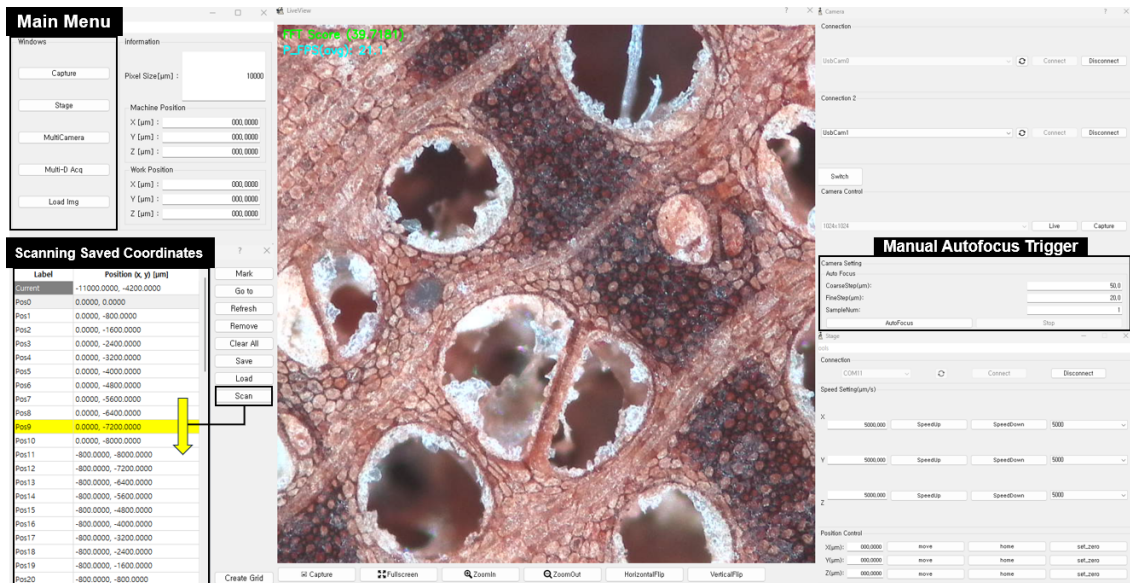


Fig. 6. Graphical user interface for automatic microscope image acquisition and stage control.

calculated DOF, the hill-climbing search halts, ensuring efficient operation while maintaining image sharpness.

3. RESULTS and DISCUSSION

In this experiment, we evaluated the performance of our GPU-accelerated FFT-based sharpness metric for the identification of various wood specimens. Specifically, we tested whether our autofocus method could find precise Z-axis locations in various samples, and how fast this method could scan multiple specimens.

The Fig. 7 shows 12 sequential images per sample

captured at $1,024 \times 1,024$ resolution using our $4 \times / 0.13$ phase-contrast objective lens and the USB camera module. In our five-sample run, the system acquired 200 images in approximately 18 min and 20 s. The CNC stage stepped the Y-axis 10 times ($800 \mu\text{m}$ each) then shifted the X-axis and repeated the process, yielding 40 images per specimen.

After initializing the prefocus sequence for each sample, each coordinate required an average of 6.61 seconds to achieve an optimal focus position. More critically, the autofocus accuracy never exceeded $\pm 10 \mu\text{m}$ deviation, which is well within the DOF, regardless

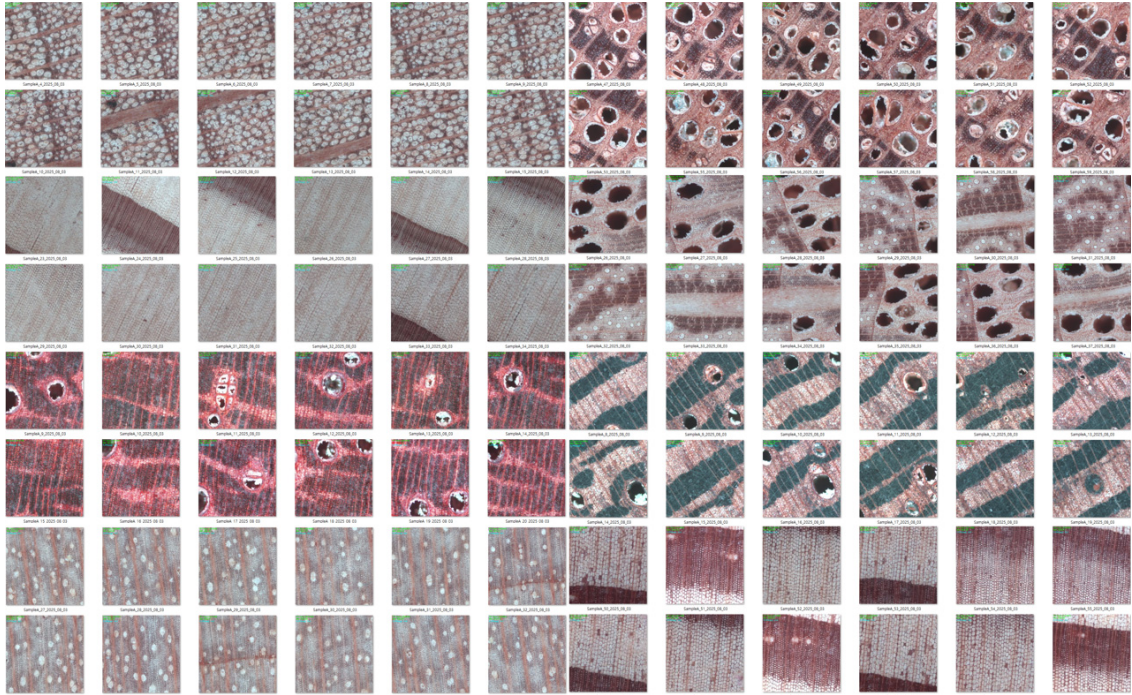


Fig. 7. Examples of sequential autofocus scanning capture of various wood specimens over adjacent X-Y positions, demonstrating consistent focus despite variations in sample surface topography. All images were acquired using the Nikon Plan 4×0.13 phase objective, whose diffraction-limited depth of focus, from the simplified approximation $\Delta z \approx \lambda / (2NA^2)$ with $\lambda \approx 0.55 \mu\text{m}$, is about $\Delta z \approx 16.27 \mu\text{m}$ in the air. Representative microscopic snapshots of various wood species under the proposed FFT-based autofocus system of the *Fagus grandifolia*, *Cryptomeria japonica*, *Pterocarpus soyauxii*, *Acer saccharum*, *Tectona grandis*, *Quercus* spp. *Milletia laurentii*, and *Larix kaempferi* were shown, arranged in rows 1–8 in the order listed. FFT: fast Fourier transform.

of wood anatomy or surface unevenness. This repeatable performance confirmed that our FFT-based metric robustly locks onto true defocus rather than native high-frequency textures across a variety of sample types.

Each move triggered a GPU-accelerated FFT score calculation, forming a closed loop of stage motion, image capture, score computation, and direction decision in near-real time.

By overlapping the data transfer and kernel execution on CUDA streams and reusing the FFT plans, our GPU pipeline reduced the planning overhead by over 90%. Compared to CPU-only implementation, the end-to-end throughput was more than three times faster, achieving approximately 18 fps for combined focus detection.

Although the FFT excels in processing individual and static frames, our five-sample benchmark showed similar scan times on the CPU and GPU (18 min); the true strength of the GPU lies in continuous, real-time analysis. By grabbing each frame “on the fly,” feeding it directly into a reusable FFT plan, as a future work layering a lightweight wavelet transform for multi-scale feature extraction could be used while sustaining the number of frames per second. This provides an avenue for achieving true real-time focus without pausing the motor movement (Table 1).

4. CONCLUSIONS

In this study, the core of our system met the need for a robust sharpness measurement algorithm that can reliably distinguish true focus from spurious texture

across the highly uneven and intricate surfaces of wood specimens. A key technical challenge addressed in this study was differentiating genuine defocus from native high-frequency features in the wood microstructure. By isolating the relevant frequency bands, our FFT-based sharpness metric successfully distinguishes true blur from structural texture. This selective sensitivity is essential to ensure a consistent focus with anatomically complex specimens. This capability underpins the ability of the system to generate uniformly sharp images across species, even for field deployment.

To keep pace with the scanning stage and avoid bottlenecks, all FFT computations, including plan generation, data transfer, and spectral masking, were fully offloaded to the GPU using pinned memory transfers, non-blocking CUDA streams, and plan caching. This pipeline achieved the throughput necessary for a continuous focus evaluation at 18 fps or higher.

To ensure that non-specialist operators could harness this technology in the field, we wrapped the autofocus routines within an intuitive graphical interface. With a clean layout for parameter tuning (motor control, threshold levels, and coarse/fine step sizes), and live visual indicators of the current focus score and stage position, users can configure, monitor, and troubleshoot the autofocus process without writing code or diving into low-level GPU settings.

In addition, to address the uneven image quality caused by frame-to-frame brightness variations during continuous capture, implementing an image-stitching pipeline—first aligning and merging overlapping frames,

Table 1. Comparison of CPU-only and GPU-accelerated pipeline performance metrics

Performance metric	CPU-only implementation	GPU-accelerated pipeline	Improvement
FFT planning overhead	100%	≈ 10%	≈ 90%
5 Samples scanning time	≈ 18 min	≈ 18 min	≈ 0%
Frames per second	≈ 6 fps	≈ 18 fps	≈ 300%

FFT: fast Fourier transform.

and then normalizing and correcting their brightness to generate a single, seamless, high-quality composite—could be considered in future work (Mohammadi *et al.*, 2024).

Moreover, because our FFT-based sharpness metric operates purely in the frequency domain and cannot capture temporal information, we will investigate it using a discrete wavelet transform (DWT) in the future (Yang *et al.*, 2025). By decomposing each frame into both time and frequency, DWT should allow us to identify and skip moments, for example, during motor-induced vibrations, when the image quality briefly degrades, and instead select and store only the fine-focused frames at each timestamp.

By meeting these requirements, the proposed autofocus technique lays the foundation for automated, large-scale wood imaging workflows, strengthening enforcement against illegal logging, and the generation of comprehensive anatomical datasets. Given its modular architecture and reliance on low-cost components, the proposed autofocus system can be readily retrofitted into existing laboratory- or field-grade wood-imaging setups, thereby providing an affordable pathway for high-throughput anatomical analysis. Beyond its technical contributions, such reliability in imaging can also support broader societal goals, as public surveys have shown that confidence in wood as an ecofriendly and health-promoting material strongly influences its cultural adoption (Han and Yang, 2022).

One limitation is that although GPUs are well-suited for streaming, our current pipeline still follows a sequential per-frame pattern (capture → host transfer → FFT scoring → idle), which prevents overlap between computation and data movement. In addition, repeated transfers between the CPU and the GPU introduce I/O bottlenecks. For future large-scale or real-time deployments, we plan to adopt a more GPU-friendly streaming design to minimize host-device traffic and enable true end-to-end concurrency.

CONFLICT of INTEREST

No potential conflict of interest relevant to this article was reported.

ACKNOWLEDGMENT

This research was funded by the Korea Forestry Promotion Institute (KOFPI) (Project No. 2023498B10-2425-AA02) and the BK FOUR Global Smart Farm Educational Research Center, Seoul National University, Seoul, Korea (Project No. A0453-20250100).

REFERENCES

- Arisandi, R., Nugroho Marsoem, S., Pramana Gentur Sutapa, J., Lukmandaru, G. 2023. The methods for measuring the area of heartwood and sapwood. *Reviews in Agricultural Science* 11: 76-92.
- Batjargal, B.U., Lee, T., Cho, M., Lee, C.J., Yeo, H. 2023. Effects of pretreatment for controlling internal water transport direction on moisture content profile and drying defects in large-cross-section red pine round timber during kiln drying. *Journal of the Korean Wood Science and Technology* 51(6): 493-508.
- Bednarski, B., Jackiewicz, K., Gałeczki, A. 2021. Influence of microstepping signal shape on shaft movement precision and torque variation of the stepper motor. *Energies* 14(19): 6107.
- Changela, A., Zaveri, M., Verma, D. 2020. FPGA implementation of high-performance, resource-efficient Radix-16 CORDIC rotator based FFT algorithm. *Integration* 73: 89-100.
- Chen, C.Y., Hwang, R.C., Chen, Y.J. 2010. A passive auto-focus camera control system. *Appl Soft Comput* 10(1): 296-303.
- Hadi, Y.S., Herliyana, E.N., Pari, G., Pari, R., Abdillah, I.B. 2022. Furfurylation effects on discoloration and

- physical-mechanical properties of wood from tropical plantation forests. *Journal of the Korean Wood Science and Technology* 50(1): 46-58.
- Han, Y., Yang, M.S. 2022. Investigation on the awareness and preference for wood culture to promote the values of wood: III. Living environment and trend of wood utilization. *Journal of the Korean Wood Science and Technology* 50(6): 375-391.
- Hwang, S.W., Sugiyama, J. 2021. Computer vision-based wood identification and its expansion and contribution potentials in wood science: A review. *Plant Methods* 17(1): 47.
- Jia, D., Zhang, C., Wu, N., Zhou, J., Guo, Z. 2022. Autofocus algorithm using optimized Laplace evaluation function and enhanced mountain climbing search algorithm. *Multimedia Tools and Applications* 81(7): 10299-10311.
- Kartikawati, E., Bienitta, Prastiwi, F.W., Nugroho, W.D. 2024. Determination of the boundary between juvenile-mature wood of *Diospyros kaki* and their wood anatomical variations. *Journal of the Korean Wood Science and Technology* 52(2): 191-203.
- Kim, K.H., Lee, H.M., Lee, M. 2024. Evaluation of adhesive characteristics of mixed cross laminated timber (CLT) using yellow popular and softwood structural lumbers. *Journal of the Korean Wood Science and Technology* 52(1): 58-69.
- Kwon, O., Lee, H.G., Lee, M.R., Jang, S., Yang, S.Y., Park, S.Y., Choi, I.G., Yeo, H. 2017. Automatic wood species identification of Korean softwood based on convolutional neural networks. *Journal of the Korean Wood Science and Technology* 45(6): 797-808.
- Kwon, O., Lee, H.G., Yang, S.Y., Kim, H., Park, S.Y., Choi, I.G., Yeo, H. 2019. Performance enhancement of automatic wood classification of Korean softwood by ensembles of convolutional neural networks. *Journal of the Korean Wood Science and Technology* 47(3): 265-276.
- Li, Z., Zhou, X., Wang, Y., Huang, G., Liu, S., Gao, B., Liu, Z. 2024. Flexible and universal autofocus based on amplitude difference of fractional Fourier transform. *Optics and Lasers in Engineering* 175: 107991.
- Lin, Y.W., Chiu, C.F., Chen, L.H., Ho, C.C. 2024. Real-time dynamic intelligent image recognition and tracking system for rockfall disasters. *Journal of Imaging* 10(4): 78.
- Mohammadi, F.S., Mohammadi, S.E., Mojarad Adi, P., Mirkarimi, S.M.A., Shabani, H. 2024. A comparative analysis of pairwise image stitching techniques for microscopy images. *Scientific Reports* 14(1): 9215.
- Nugroho, W.D., Na'Iem, M., Lukmandaru, G., Widiyatno, Feriawan, Y., Prastiwi, F.W., Wibowo, A., Puspitasari, D. 2024. Physical and mechanical properties of 20-year-old clonal teak trees in Ngawi, East Java, Indonesia. *Journal of the Korean Wood Science and Technology* 52(5): 459-472.
- Park, Y., Kim, C., Jeong, H., Lee, H.M., Kim, K.M., Lee, I.H., Kwon, G.B., Yoon, N., Lee, N. 2024. Evaluation of the basic properties for the Korean major domestic wood species: I. Korean red pine (*Pinus densiflora*) in Pyeongchang-gun, Gangwon-do. *Journal of the Korean Wood Science and Technology* 52(1): 87-100.
- Peddigari, V., Gamadia, M., Kehtarnavaz, N. 2005. Real-time implementation issues in passive automatic focusing for digital still cameras. *Journal of Imaging Science and Technology* 49(2): 114-123.
- Ravindran, P., Thompson, B.J., Soares, R.K., Wiedenhoeft, A.C. 2020. The XyloTron: Flexible, open-source, image-based macroscopic field identification of wood products. *Frontiers in Plant Science* 11: 1015.
- Silva, N.R.D., Deklerck, V., Baetens, J., den Bulcke, J.V., De Ridder, M., Rousseau, M., Bruno, O.M., Beeckman, H., Acker, J.V., De Baets, B., Verwaeren, J. 2022. Improved wood species identification based

- on multi-view imagery of the three anatomical planes. *Plant Methods* 18: 79.
- Sutapa, J.P.G., Lukmandaru, G., Sunarta, S., Pujiarti, R., Irawati, D., Arisandi, R., Dwiyantha, R., Priyambodo, R.D. 2024. Utilization of sapwood waste of fast-growing teak in activated carbon production and its adsorption properties. *Journal of the Korean Wood Science and Technology* 52(2): 118-133.
- Wu, X., Zhou, H., Yu, H., Hu, R., Zhang, G., Hu, J., He, T. 2022. A method for medical microscopic images' sharpness evaluation based on NSST and variance by combining time and frequency domains. *Sensors* 22(19): 7607.
- Yang, W., Lv, M., Yu, Z., Deng, J. 2025. A wavelet-guided transformer approach for autofocus in brightfield biological microscopy. *Scientific Reports* 15(1): 25521.
- Yoo, H.J., Kwon, O., Seo, J.W. 2022. Mask region-based convolutional neural network (R-CNN) based image segmentation of rays in softwoods. *Journal of the Korean Wood Science and Technology* 50(6): 490-498.
- Young, I.T., Zagers, R., van Vliet, L.J., Mullikin, J., Boddeke, F., Netten, H. 1993. Depth-of-focus in microscopy. In: Tromso, Norway, SCIA'93, Proceedings of the 8th Scandinavian Conference on Image Analysis, pp. 493-498.
- Zeitlin, J., Overdevest, C. 2021. Experimentalist interactions: Joining up the transnational timber legality regime. *Regulation & Governance* 15(3): 686-708.
- Zinad, O.S., Csiha, C. 2024. Review on water vapor diffusion through wood adhesive layer. *Journal of the Korean Wood Science and Technology* 52(4): 301-318.